Vol. 10 • No. 9 • March 24 • 2023
www.advmatinterfaces.de

ADVANCED MATERIALS INTERFACES

Open Access

21967350, 2023, 9, Downloaded from https://onlinelibrary.wiley.com/doi/10.1002/admi.202370030, Wiley Online Library on [24/03/2023]. See the Terms and Conditions (https://onlinelibrary.wiley.com/terms-and-conditions) on Wiley Online Library for rules of use; OA articles are governed by the applicable Creative Commons License

WILEY VCH

ADVANCED MATERIALS INTERFACES
Open Access
www.advmatinterfaces.de

Check for updates

Influence of a Tailored Oxide Interface on the Quality Factor of Microelectromechanical Resonators

David D. Lynes and Hengky Chandrahalim**

Piezoelectric microelectromechanical systems (MEMS) are used as sensors, actuators, energy harvesters, accelerometers, and communication modules. Aluminum nitride (AlN) is an especially attractive piezoelectric material because its fabrication process allows it to be integrated into semiconductor circuitry to deliver a fully integrated solution. Microelectromechanical resonators with AlN sandwiched between n-type silicon (Si) and top metal electrode with and without a silicon oxide layer are designed and fabricated. The effect of the oxide film is up to a fourfold increase in quality factor (*Q*) that is consistent from very high frequency (VHF) to super high frequency (SHF). This effect is demonstrated using thin plate bulk acoustic wave modes from 70–80 MHz using the second contour mode and first width extensional mode and from 9.5–10.5 GHz using high overtone thickness modes. To explore potential applications of AlN-transduced *Q*-enhanced MEMS devices in harsh environments, measurements from −200 °C to +200 °C are performed. The *Q* enhancement is persistent across a wide temperature range for both VHF and SHF resonators with the added oxide layer. Furthermore, AlN-on-Si resonators that have a comparable temperature coefficient of frequency to silicon carbide-based resonators in commercial applications are demonstrated.

1. Introduction

Piezoelectric materials have been widely used to facilitate efficient electromechanical transductions in a variety of important applications ranging from energy harvesting,[1–3] signal processing,[4–6] health,[7–9] automotive,[10,11] robotics,[12,13] to defense and aerospace environments.[14,15] When compared to other common microelectromechanical systems (MEMS) transduction methods such as thermal/piezoresistive,[16–18] capacitive,[19–22] and electrostatic[23–25] schemes, piezoelectric materials have a higher energy density, better frequency scaling, lower power configurations, and are easier to characterize and integrate.[19,26,27] Additionally, it is possible to include additives in many piezoelectric materials to modify material properties such as acoustic velocity, dielectric constant, quality factor, electromechanical coupling, as well as temperature and aging characteristics[28] or ferroelectric properties.[29] Some piezoelectric materials have desirable semiconductor properties.[30–32] The fabrication processes for many piezoelectric thin films allow them to be integrated into complementary metal oxide semiconductor (CMOS) circuitry to deliver a fully integrated solution.[19]

Piezoelectrically transduced microscale resonant devices have broad applications such as inertial sensing,[33–36] radio frequency (RF) signal processing,[37–43] and environmental monitoring.[44,45] Within these fields, microscale piezoelectric resonators are widely used in various applications like frequency filtering, sensing, and clock generation.[46] Piezoelectric resonators are able to cover a broad frequency range and are able to actuate many vibrational modes such as extension, thickness, shear, and flexure. They are able to achieve high selectivity, narrow bandwidth, and good stability. The use of piezoelectrically transduced resonators in filters for radio applications has been commonplace since the 1970s. Early applications included amplitude modulation radio and telephone filters, frequency shift keying filters, and filters for early radio navigation receivers such as Loran-C and Omega.[28] Modern micro- and nano-scale resonators are now commonplace in very high frequency (VHF) applications. Continued miniaturization, low cost, and CMOS compatibility have made piezoelectric MEMS resonators an ideal candidate for use in ultra- and super-high frequency (UHF, SHF) applications such as duplexers in smartphones and Wi-Fi filters. As hand-held and internet of things devices continue to shrink, the lightweight, low power, high-frequency range, and multimode characteristics of micro- and nano-scale resonators have made them the focus of much research.[46]

Aluminum nitride (AlN) is an especially attractive piezoelectric material. In its thin film form, AlN retains most of its bulk physical, thermal, and electric properties. The low-temperature requirement (<400 °C) for the sputtering deposition of AlN makes it an ideal choice for CMOS-integrated transducers.[47–52] Another advantage of AlN is that it does not contaminate the cleanroom environment or equipment (unlike lead zirconate titanate, also known as PZT, due to its lead

D. D. Lynes, H. Chandrahalim
Department of Electrical and Computer Engineering
Air Force Institute of Technology
Wright-Patterson Air Force Base, Dayton, OH 45433, USA
E-mail: david.lynes.2@au.af.edu; hengky@microsystems.group

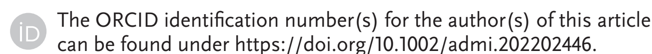
The ORCID identification number(s) for the author(s) of this article can be found under https://doi.org/10.1002/admi.202202446.

© 2023 The Authors. Advanced Materials Interfaces published by Wiley-VCH GmbH. This is an open access article under the terms of the Creative Commons Attribution License, which permits use, distribution and reproduction in any medium, provided the original work is properly cited.

DOI: 10.1002/admi.202202446

 © 2023 The Authors. Advanced Materials Interfaces published by Wiley-VCH GmbH

21967350, 0, Downloaded from https://onlinelibrary.wiley.com/doi/10.1002/admi.202202446 by D'Azzo Research Library, Wiley Online Library on [13/02/2023]. See the Terms and Conditions (https://onlinelibrary.wiley.com/terms-and-conditions) on Wiley Online Library for rules of use; OA articles are governed by the applicable Creative Commons License

ADVANCED MATERIALS INTERFACES
Open Access
www.advmatinterfaces.de

21967350, 0, Downloaded from https://onlinelibrary.wiley.com/doi/10.1002/admi.202202446 by D'Azzo Research Library, Wiley Online Library on [13/02/2023]. See the Terms and Conditions (https://onlinelibrary.wiley.com/terms-and-conditions) on Wiley Online Library for rules of use; OA articles are governed by the applicable Creative Commons License

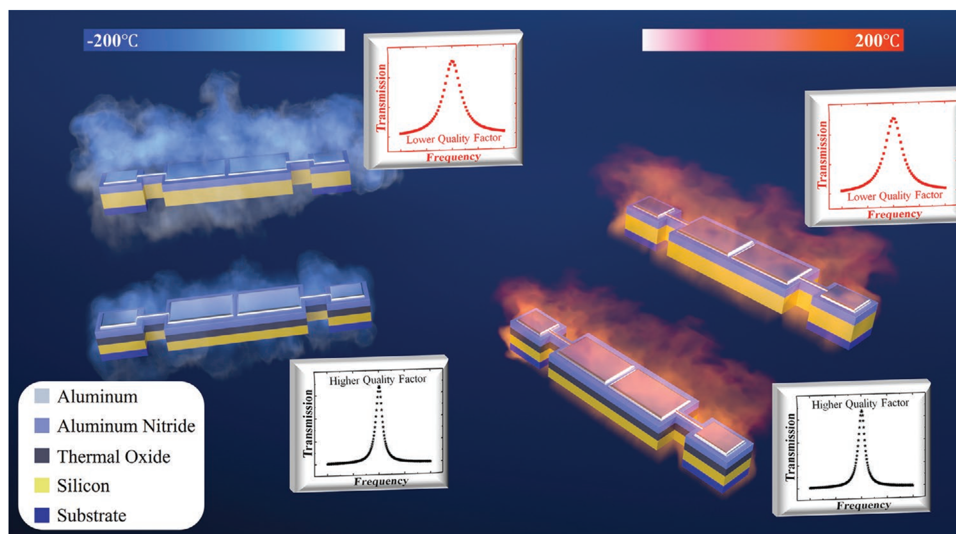

Figure 1. The resonators with a thin oxide film show consistent Q enhancement regardless of the modes of vibrations in the VHF range over a 400 °C range of temperature. The TCF at room temperature was ≈−30 ppm °C^{-1} for the VHF resonators and −35 ppm °C^{-1} for the SHF resonators. We have demonstrated AlN resonators on a silicon substrate that have comparable TCF to SiC.[62]

content) and it does not require a post-deposition poling step.[47] Furthermore, AlN can be doped with scandium to increase electromechanical coupling while maintaining a high quality (Q) factor[53] or to add ferroelectric behavior.[54] As a piezoelectric, AlN has been successfully implemented in transducers for a wide range of devices including energy harvesters, acoustic devices, sensors, actuators, RF filters and duplexers,[47,55,56] and accelerometers.[14] AlN has also been successfully implemented as part of the gate dielectric in thin film transistors.[57] The integration of CMOS and MEMS devices on a single chip reduces die size, power consumption, and manufacturing costs.[47]

In many applications, it is most important that the piezoelectrically transduced resonant devices have extremely high Q. A narrower bandwidth at resonance enables a higher sensitivity and resolution for precision sensing tasks. High Q resonant devices have a lower loss for signal processing and energy harvesting. Lower loss results in a strong signal in RF processing and higher output in energy harvesting applications. In general, the lower Q the resonator has, the higher the system noise and interference.[19] Q enhancement has focused on reducing both intrinsic losses from material and resonator dimensions and extrinsic losses such as support and air/fluid losses. Enhancement methods include the use of phononic crystals, dispersion-engineered resonators, support transducer topologies, micromachined reflectors,[19] and doping.[53]

Largely due to their small size and low power consumption, these devices are seen as well suited for aerospace and power applications. Piezoelectric accelerometers used in inertial sensors for air and spacecraft navigation systems are subject to extreme vibration and loading. Resonant devices in spacecraft communication systems are subject to large temperature fluctuations (−230 °C to +180 °C)[58] and a wide range of radiations (electron, proton, neutron, and electromagnetic).[59] Piezoelectric sensors used for temperature and vibration monitoring[14] in nuclear reactors are exposed to extreme gamma and neutron radiation. Significant research has gone into demonstrating these devices maintain functionality these in harsh thermal,[60] pressure,[61] and radiation environments.[14]

We designed AlN transduced thin plate resonators with and without a silicon oxide (SiO_2) layer. FEA harmonic analysis is used to predict resonant frequencies and mode shapes of the two designs. The designs were sent to a commercial foundry, MEMSCap, for fabrication. To explore potential applications of these devices in harsh environments, we performed RF characterization from −200 °C to +200 °C as illustrated in **Figure 1**. The effect of the added oxide layer is up to a fourfold increase in Q that is consistent across a wide frequency range (VHF–SHF) and temperature range. This effect is demonstrated using bulk acoustic wave (BAW) modes from 70–80 MHz using the second contour mode (CM) and first width extensional mode (WEM) and from 9.5–10.5 GHz using high overtone thickness modes (TM). Furthermore, we have demonstrated AlN resonators on a silicon substrate that have a comparable temperature coefficient of frequency (TCF) to silicon carbide (SiC).[62] The TCF at room temperature was ≈−30 ppm °C^{-1} for the VHF resonators and −35 ppm °C^{-1} for the SHF resonators. TCFs of less than ±50 ppm °C^{-1} are considered suitable for time-keeping in handheld wireless devices.[63]

2. Results and Discussion

2.1. Experiment

We performed a systematic study to see the influence of thin oxide film on TCF, Q, motional resistance (R_m), and effective electromechanical factor (k_{eff}^2) of bulk mode resonators. We chose rectangular thin-plate resonators for this study. The rectangular thin-plate resonators are designed to be driven in different BAW modes by applying an RF signal across the top and bottom electrodes thereby activating the d_{31}[64,65] or d_{33} vibrational modes in the AlN. The specific BAW vibrations investigated in this work are the first WEM, second contour

© 2023 The Authors. Advanced Materials Interfaces published by Wiley-VCH GmbH

ADVANCED MATERIALS INTERFACES
Open Access
www.advmatinterfaces.de

21967350, 0, Downloaded from https://onlinelibrary.wiley.com/doi/10.1002/admi.202202446 by D'Azzo Research Library, Wiley Online Library on [13/02/2023]. See the Terms and Conditions (https://onlinelibrary.wiley.com/terms-and-conditions) on Wiley Online Library for rules of use; OA articles are governed by the applicable Creative Commons License

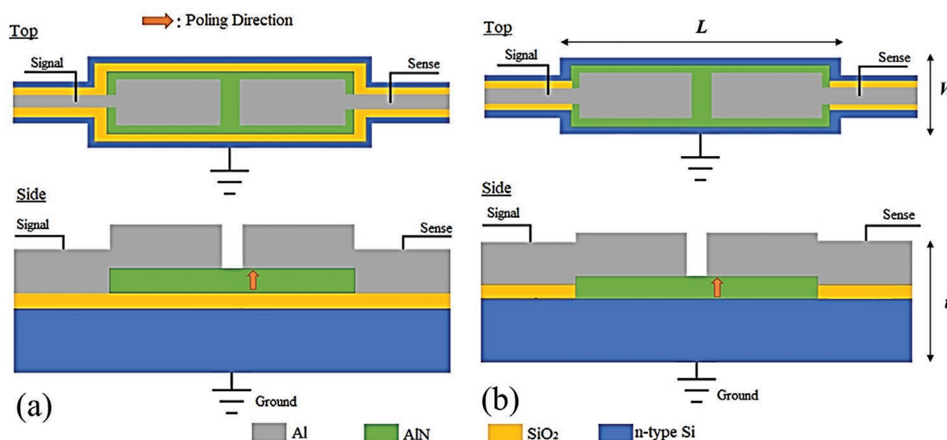

Figure 2. Schematic of a) AlN-on-SiO_2 and b) AlN-on-Si rectangular thin plate resonators. The critical dimensions are labeled: length (L), width (W), and thickness (t).

mode (CM),[28] and high overtone TM. The first WEM and second CM vibrations are in-plane and the high overtone TM vibrations are out of the plane. The layout and key dimensions of the rectangular flat plate resonator are presented in **Figure 2**. The frequency equation for rectangular plate CM vibrations is given by the transcendental equation:[28]

$$\frac{\cot\left(\alpha\frac{W}{2}\right)}{\cot\left(\beta\frac{W}{2}\right)}=\frac{-2\alpha\beta k^2(1-\mu)}{(\beta^2-k^2)(\alpha^2+\mu k^2)} \quad (1)$$

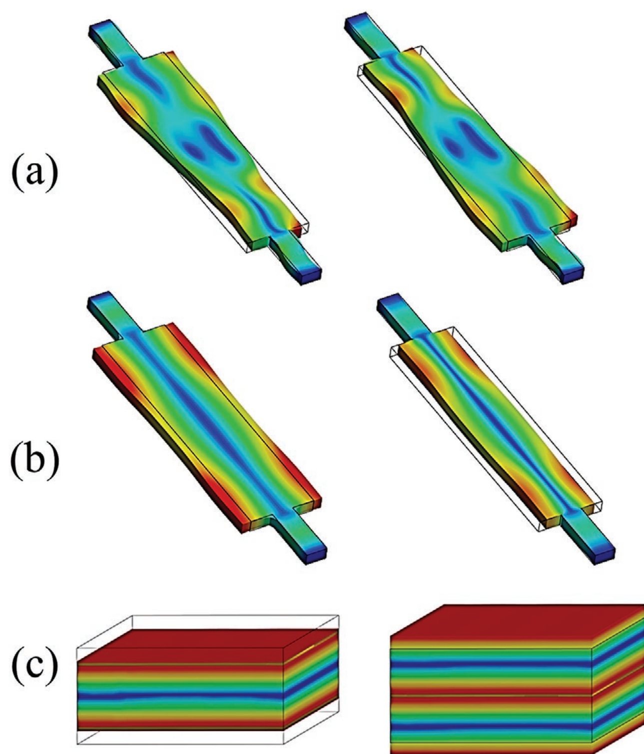

Figure 3. Qualitative examples of motion for a) the second CM, b) the first WEM, and c) the third TM.

where

$$\alpha^2=\frac{(1-\mu)\theta^2}{2}-k^2 \qquad \beta^2=\theta^2-k^2 \quad (2)$$

$$\theta^2=\frac{2\rho_{eq}\omega^2(1+\mu_{eq})}{E_{eq}} \qquad k=\frac{\pi}{L} \quad (3)$$

and E_{eq}, ρ_{eq}, and μ_{eq} are the equivalent Young's modulus, equivalent density, and equivalent Poisson's ratio of the material stack suspended in the resonator, respectively. W and L are the width and length of the rectangular plate, respectively, and ω is the angular frequency. In the case where $L \gg W$, the solution to the rectangular plate CM converges such that the resonance frequency (f_r) of the can be approximated by:[19,38,46]

$$f_r=\frac{\kappa}{2W}\sqrt{\frac{E_{eq}}{\rho_{eq}}} \quad (4)$$

where κ is a dimensionless constant that is dependent upon the mode shape.[19] When $\kappa = n$, Equation (2) predicts the resonant frequency for the nth WEM vibration. The same approximation may be made for the nth TM vibration by replacing W with thickness, t.[19] Qualitative illustrations of the vibrational modes are presented in **Figure 3**.

FEA simulations were accomplished with Ansys Mechanical to predict the resonant frequency and mode shapes using the material properties presented in Table S1 (Supporting Information). The BAW vibrational modes and their corresponding resonant frequencies are presented in Table S2 (Supporting Information).

The resonator designs were built using MEMSCap's PiezoMUMPs fabrication process (see Figure S4, Supporting Information section).[66] The resonators built for the experiment were designed to not exceed a 400 × 200 µm footprint, to include the contact electrodes. The resonators are suspended in the air by two anchors and are ≈220 × 60 µm across and 12 µm thick. The rectangular thin plate consists of a 10 µm thick n-type Si (100) layer with a 0.5 µm thick AlN transduction

 © 2023 The Authors. Advanced Materials Interfaces published by Wiley-VCH GmbH

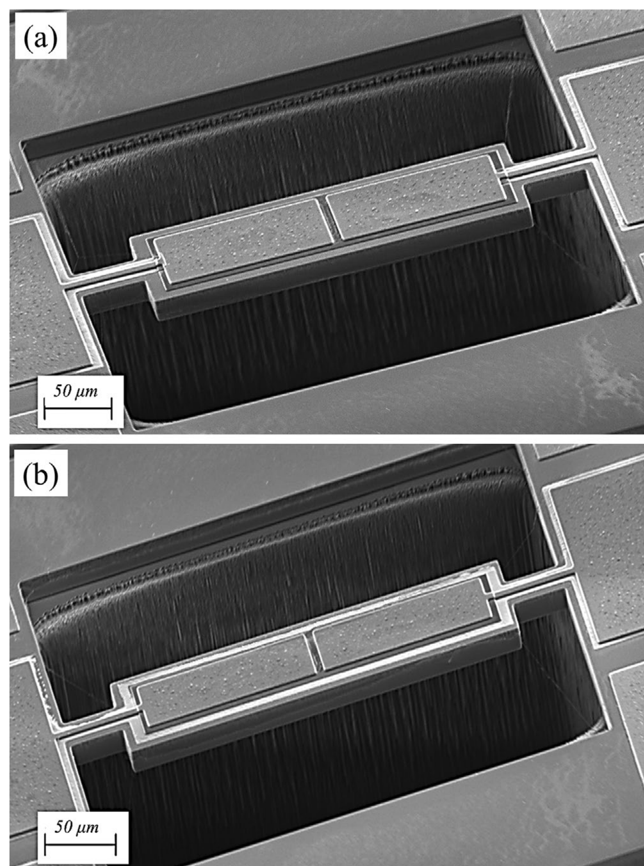

Figure 4. Scanning electron micrographs of a) AlN-on-Si and b) AlN-on-SiO_2 rectangular thin plate resonators fabricated by MEMSCap.

layer. The structural n-Si also acts as the bottom conductor. A 1.0 µm Al and 20 nm chrome (Cr) stack is used as the top electrode. We designed devices with and without an oxide layer such that the top electrode and AlN layers were identical. Scanning electron micrographs of the completed resonators are presented in **Figure 4**. The first design has the SiO_2 layer sandwiched between the AlN and Si (Figure 4b), and the second only uses the SiO_2 as an insulation layer between the top and bottom electrodes (Figure 4a). The device dimensions are summarized in **Table 1**. Cross-sectional SEM images of the devices are provided in Figure S5 (Supporting Information) section. The imagery shows the Al, Cr, AlN, SiO_2, and n-Si layers are uniform and well-defined.

Two-port scattering parameters (S-parameters) of the resonators operating in the different modes were measured under vacuum using a Lake Shore cryogenic probe station. An Agilent/Keysight N5222A PMA microwave network analyzer was used to record the S-parameters. The two-port S-parameters were recorded in 10 °C increments from −200 °C to +200 °C at 1.0 (±0.3) µTorr. The network analyzer RF input power was 0 dBm. Two-port short-open-load-through calibration was accomplished to correct line and probe errors. Three randomly selected AlN-on-SiO_2 resonators and three AlN-on-Si resonators were measured to capture variance. An illustration of the experimental setup is presented in **Figure 5**.

S-parameter data was post-processed to measure f_r, Q, motional resistance (R_m), and one port effective electromechanical factor (k_{eff}^2). Q was measured using:[46]

$$Q = \frac{f_r}{BW_{3dB}} \tag{5}$$

where BW_{3dB} is the bandwidth at 3 dB less than the peak. R_m and one port k_{eff}^2 were calculated using the following equations, respectively:[19,46]

$$R_m = 2Z_o\left(10^{-\frac{IL}{20}} - 1\right) \tag{6}$$

$$k_{\mathrm{eff}}^2 = \frac{\left(f_a^2 - f_r^2\right)}{f_r^2} \tag{7}$$

where Z_o is the termination impedance, IL is the insertion loss at the resonant frequency, and f_a is the frequency at anti-resonance. The temperature coefficient of frequency (TCF) is calculated using:[46]

$$\mathrm{TCF} = \frac{1}{f_r}\frac{\partial f_r}{\partial T} \tag{8}$$

where T is temperature, and the units of TCF are presented as ppm °C^{-1}.

2.2. VHF Vibrational Modes

S-parameters were experimentally measured for VHF resonant modes of the rectangular flat plate from −200 °C to +200 °C at 1.0 (±0.3) µTorr. Mode shapes and resonant frequencies were predicted using FEA harmonic analysis. The FEA harmonic analysis of the VHF regime is presented in Figure S3a (Supporting Information). Extensional and contour modes are dominant in the VHF regime. Illustrations of the second CM and first WEM are provided in Figure S1 (Supporting Information). As a general trend, R_m for the first WEM is greater than that of the second CM. In both modes f_r and Q decrease and R_m increases as temperature increases. Q values of the resonator with the oxide layer are consistently greater than those of the

Table 1. Fabricated resonator dimensions. Dimensions are in µm.

Resonator design	Top electrodes [$L \times W \times t$]	AlN layer [$L \times W \times t$]	SiO_2 layer [$L \times W \times t$]	Si layer [$L \times W \times t$]
Without oxide layer	97 × 37 × 1.02	206 × 46 × 0.5	Not applicable	216 × 56 × 10
With oxide layer	97 × 37 × 1.02	206 × 46 × 0.5	216 × 56 × 0.2	222 × 62 × 10

© 2023 The Authors. Advanced Materials Interfaces published by Wiley-VCH GmbH

21967350, 0, Downloaded from https://onlinelibrary.wiley.com/doi/10.1002/admi.202202446 by D'Azzo Research Library, Wiley Online Library on [13/02/2023]. See the Terms and Conditions (https://onlinelibrary.wiley.com/terms-and-conditions) on Wiley Online Library for rules of use; OA articles are governed by the applicable Creative Commons License

21967350, 0, Downloaded from https://onlinelibrary.wiley.com/doi/10.1002/admi.202202446 by D'Azzo Research Library, Wiley Online Library on [13/02/2023]. See the Terms and Conditions (https://onlinelibrary.wiley.com/terms-and-conditions) on Wiley Online Library for rules of use; OA articles are governed by the applicable Creative Commons License

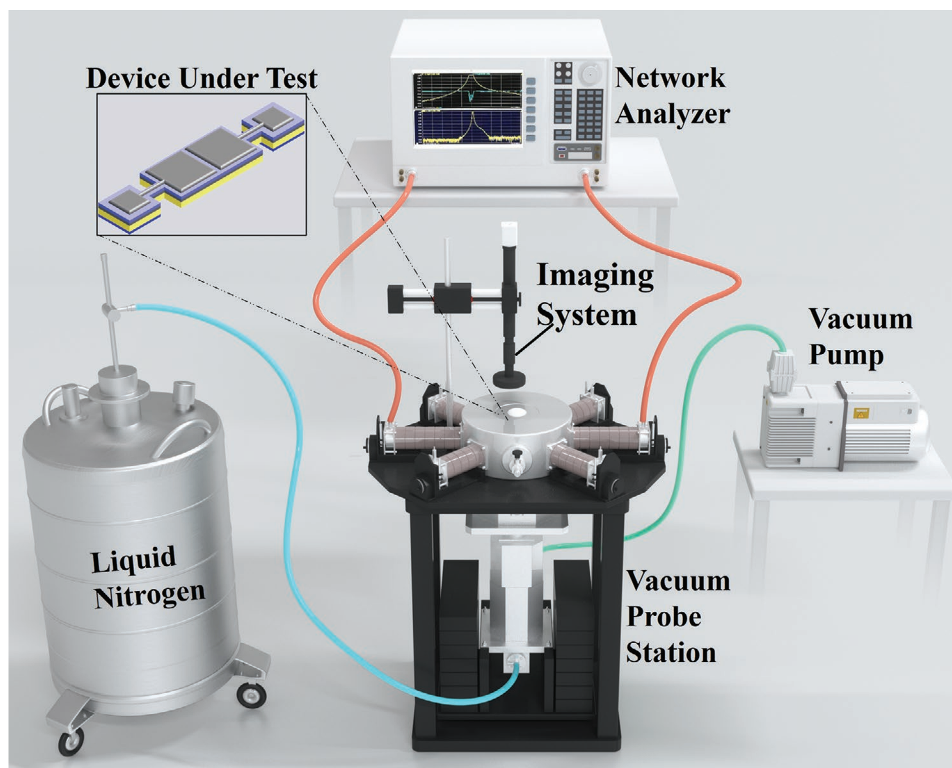

Figure 5. Illustration of the cryogenic vacuum probe station experimental setup. Liquid nitrogen brings the resonator to cryogenic temperatures as low as −200 °C. Built-in hot plates are capable of bringing the sample to +200 °C. The turbo vacuum pump maintains a nominal 1 µTorr.

device without the oxide layer, even at high temperatures. An example of the enhanced *Q*, the shift in frequency, and peak broadening with increasing temperature are clearly illustrated in **Figure 6**.

The TCF, R_m, *Q*, and one port k^2_{eff} for the first WEM vibrations from −200 °C to +200 °C are presented in **Figure 7**a–d, respectively. TCF at room temperatures are −29.8 ± 1.0 ppm °C^{-1} for the baseline resonator (no SiO_2 layer) and −31.2 ± 2.0 ppm °C^{-1}. for the resonator with the SiO_2 layer. TCF is not significantly different between the two designs across all evaluated temperatures. The SiO_2 layer increases R_m by ≈2.3 kΩ and decreases k^2_{eff} by 0.2% at room temperature. However, adding the oxide layer increases *Q* by up to 7000 points in some cases. At room temperature, *Q* for the baseline resonator is 1410 ± 810 and 8040 ± 800 for the resonator with the SiO_2 layer. The addition of the oxide layer increased *Q* by 5.7 times. Statistical analysis shows the difference in *Q* is significant within a 90% confidence interval (α = 0.1) up to +180 °C. Quality factors over 10 000 are achieved at cryogenic temperatures.

Results for the second CM are presented in **Figure 8**. Baseline TCF at room temperature is −26.4 ± 1.2 ppm °C^{-1} and −28.4 ± 1.4 ppm °C^{-1} for the device with the oxide layer. Overall, there are no significant differences in TCF behavior. Similar to the first WEM vibration, R_m is roughly doubled by adding the SiO_2 layer. The effective electromechanical coupling of the device with the SiO_2 layer is consistently below the baseline device, but the difference does not exceed the 90% confidence interval threshold of statistical significance. At room temperature, baseline *Q* is 412 ± 61. Adding the oxide layer increases *Q* to 2400 ± 250, 5.8 times greater than baseline. Statistical analysis demonstrates the *Q* enhancement is significant within a 90% confidence interval across the entire evaluated temperature range.

2.3. SHF Vibrational Modes

S-parameters were experimentally measured for SHF resonant modes of the rectangular flat plate from −200 °C to +200 °C at 1.0 (±0.3) µTorr. Mode shape and resonant frequencies were predicted using FEA harmonic analysis. The FEA harmonic analysis of the SHF regime is presented in Figure S3b (Supporting Information). In the SHF regime, the higher-order CM and WEM vibrational modes have completely decayed and the resonance is dominated by TM vibrations. The measured high overtone TM vibrations were between 9.5 to 10.5 GHz. Illustrations of the high overtone TM shapes are provided in Figure S2 (Supporting Information). As a general trend, f_r and *Q* decrease with increasing temperature. Unlike the VHF vibrational modes, R_m decreases with increasing temperature in the SHF thickness mode vibrational regime; however, the noise floor also increases. This is because the RF signal at SHF easily leaks via the feedthrough capacitance, causing the entire noise floor to go up. Some *Q* enhancement is still present, although less apparent from a qualitative perspective than the VHF vibrational modes. Notably, a high-frequency "ringing" is present in this frequency range across all measured devices. The ringing is more prevalent at lower temperatures. The magnitude of the

 © 2023 The Authors. Advanced Materials Interfaces published by Wiley-VCH GmbH

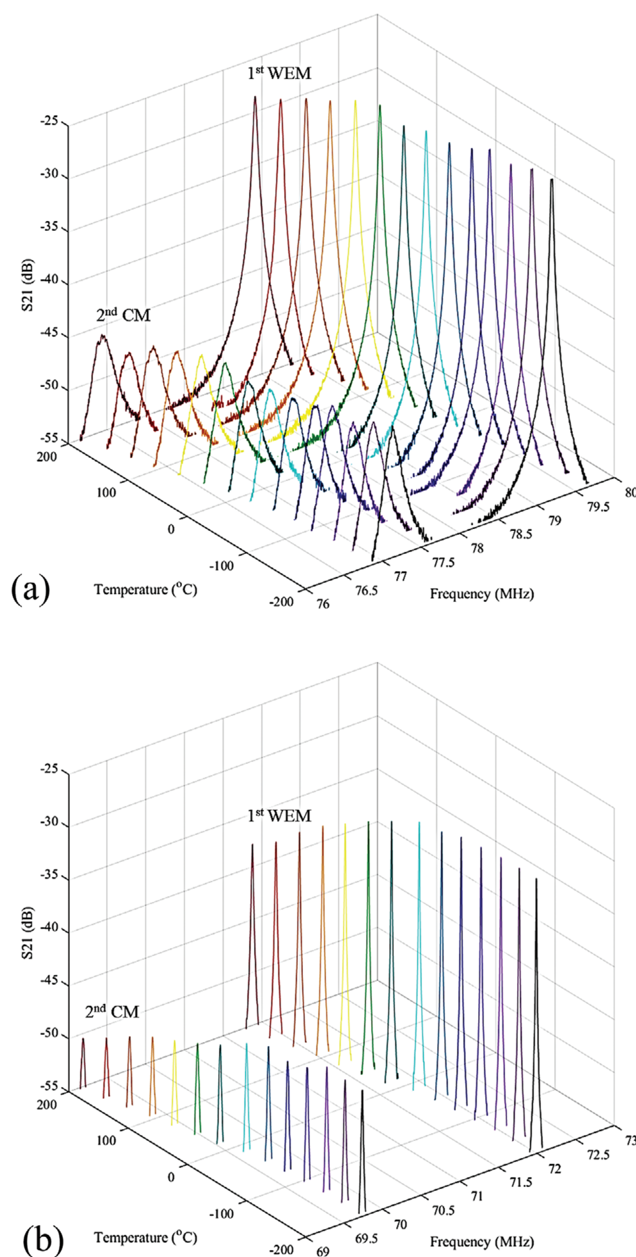

Figure 6. A measured VHF frequency response for a rectangular flat plate resonator a) without an oxide layer and b) with an oxide layer. The resonator with the oxide layer exhibits significantly greater Q for both modes. As a general trend, as the temperature increases, Q and resonant frequency decrease and R_m increases.

ringing is much smaller for the resonator with the SiO_2 layer than the device without the oxide layer. A deeper study into the reduction of the ringing in the device with an oxide layer is beyond the scope of this paper; however, it merits further investigation. The frequency shift and spurious mode damping are clearly illustrated in the example presented in **Figure 9**.

TCF, R_m, Q, and one port k_{eff}^2 were measured for the high overtone TM vibrations from –200 °C to +200 °C and 1 µTorr. These correspond to ≈9.65, 10.0, and 10.35 GHz resonant frequencies, respectively. Measured values for TCF, R_m, Q, and k_{eff}^2 at are presented in **Figure 10**, **Figure 11**, and **Figure 12** for the 9.65, 10.0, and 10.35 GHz vibrations, respectively. Across all three modes, the average TCF at room temperature was –34.0 ± 3.1 ppm °C^{-1} for the baseline device and –37.9 ppm °C^{-1} ± 4.4 for the device with the added SiO_2 layer. Similar to the first WEM and second CM vibrations, the addition of the oxide layer increased R_m, with the average baseline at 5.2 ± 0.1 kΩ and average R_m for the device with the oxide layer at 7.3 ± 0.1 kΩ at room temperature. At low temperatures, some Q enhancement was observed. Devices with an oxide layer exhibited Q as high as 700 at temperatures less than –100 °C. At similar temperatures, the highest demonstrated Q for devices without the oxide layer was 350.

2.4. Discussion

The overall Q of a system is found by summing the dissipated energies. This is more commonly written as the sum of quality factors associated with each source of loss (Q_i):[46,67,68]

$$\frac{1}{Q} = \sum_i \frac{1}{Q_i} \tag{9}$$

Sources of loss are divided into intrinsic and extrinsic sources. Intrinsic losses are solely dependent upon the materials and dimensions of the resonator and include dielectric, piezoelectric, phonon-phonon interaction, and phonon-electron interaction losses. Extrinsic losses are those losses not fundamentally bound to material properties and include anchor, fluid, surface, and ohmic losses.[46] With the exception of the added SiO_2 layer, the resonators are identical in geometry, anchor design, and environment. Therefore, we identify the primary cause of Q enhancement as an improvement in acoustic impedance mismatch between the AlN and Si layers.

The characteristic specific acoustic impedance, Z_o, is given by the product of acoustic velocity, c, and mass density.[69] Using the densities, acoustic velocities, and characteristic specific acoustic impedances as presented in **Table 2**; without the oxide layer there is a large acoustic impedance mismatch between the dielectric layer and the silicon ($|\Delta Z_o| = 12.8$). With the oxide layer, the AlN-SiO_2 dielectric layer has an average acoustic impedance of 22.8 MPa s m^{-3} ($|\Delta Z_o| = 3.1$). Thus, at VHF range, Q improves when the oxide layer is added.

Akhiezer-type phonon-phonon interaction losses become dominant in the SHF range.[46,70] Akhiezer loss describes the interaction between thermal phonons and vibrational phonons when phonon scattering time is much shorter than one period of vibration (i.e., $\tau_s \ll \tau_v$). Irreversible loss occurs as phonons interact with each other. Q_{AKE} associated with this loss is found using the formula:[46,71]

$$Q_{AKE} = \frac{\rho c^4}{2\pi f \gamma_{avg}^2 kT} \tag{10}$$

where ρ is the material density, c is the acoustic velocity, f is the frequency of vibration, γ_{avg} is the average Grünesen's parameter,

© 2023 The Authors. Advanced Materials Interfaces published by Wiley-VCH GmbH

21967350, 0, Downloaded from https://onlinelibrary.wiley.com/doi/10.1002/admi.202202446 by D'Azzo Research Library, Wiley Online Library on [13/02/2023]. See the Terms and Conditions (https://onlinelibrary.wiley.com/terms-and-conditions) on Wiley Online Library for rules of use; OA articles are governed by the applicable Creative Commons License

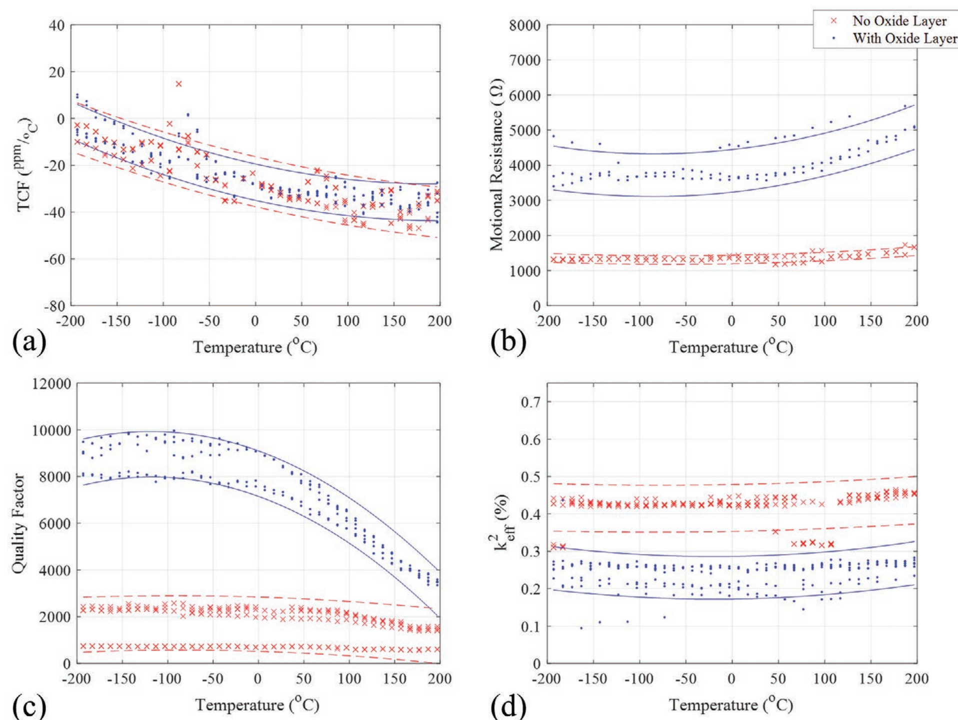

Figure 7. a) TCF, b) R_m, c) Q, and d) k^2_{eff} for the first WEM vibration of the rectangular thin plate with the SiO_2 layer and without. Boundaries indicate the 90% confidence interval.

T is temperature, and k is thermal conductivity. As frequency increases, Q_{AKE} decreases proportionally and the loss improvement given by the oxide layer is overcome by Akhiezer phonon-phonon interaction losses. This explains the dissipation of the Q enhancement for the high-overtone TM vibrations as T and f increase.

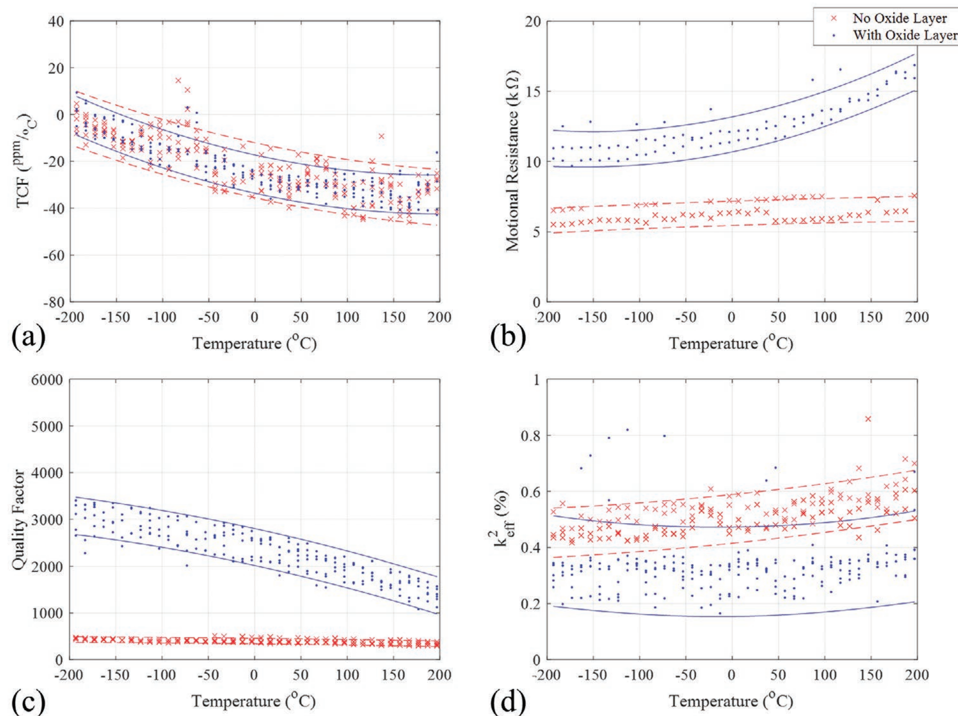

Figure 8. a) TCF, b) R_m, c) Q, and d) k^2_{eff} for the second CM vibration of the rectangular thin plate with the SiO_2 layer and without. Boundaries indicate the 90% confidence interval.

© 2023 The Authors. Advanced Materials Interfaces published by Wiley-VCH GmbH

21967350, 0, Downloaded from https://onlinelibrary.wiley.com/doi/10.1002/admi.202202446 by D'Azzo Research Library, Wiley Online Library on [13/02/2023]. See the Terms and Conditions (https://onlinelibrary.wiley.com/terms-and-conditions) on Wiley Online Library for rules of use; OA articles are governed by the applicable Creative Commons License

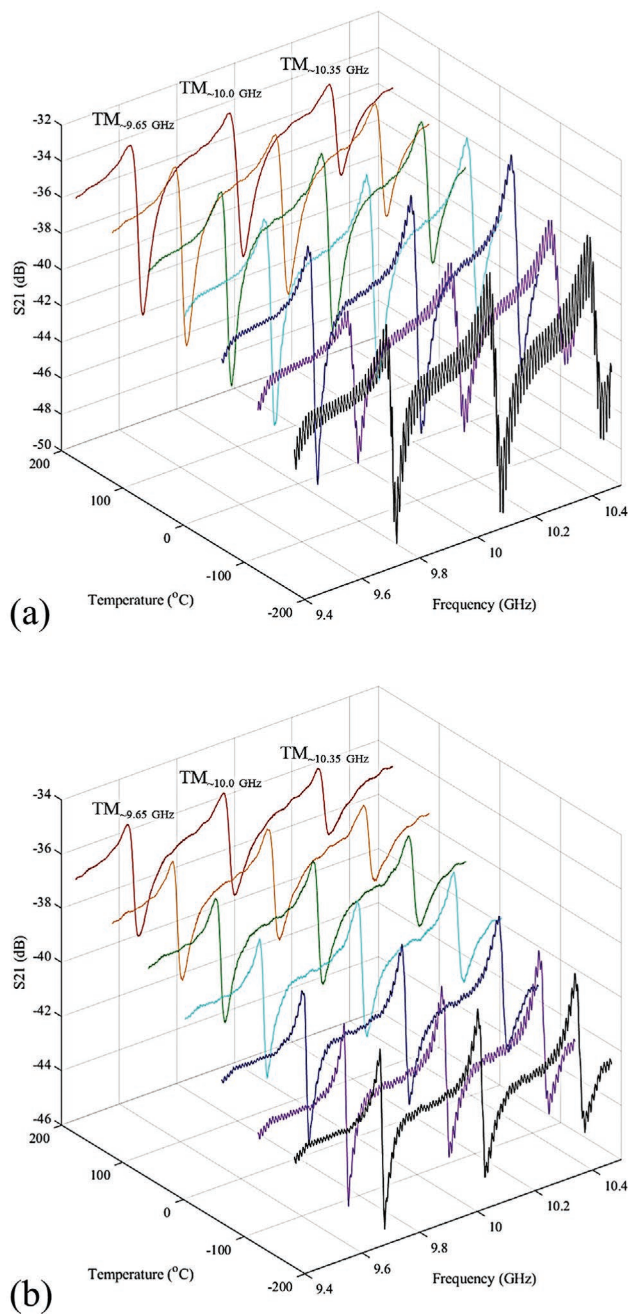

Figure 9. A measured SHF frequency response for a rectangular flat plate resonator a) without an oxide layer and b) with an oxide layer. The resonator with the oxide layer exhibits a greater Q as well as a reduction in the magnitude of the higher frequency noise.

Other loss sources such as thermoelastic damping (TED), squeeze film damping, surface losses, and air damping are less significant. TED describes the process of phonon diffusion from sections of higher temperature to lower temperature spots. TED in bulk-mode resonators is considered negligible in the frequency range for which they are utilized.[46] Squeeze film damping is negligible because there are no small air gaps around the resonator. Surface losses can be considered negligible because the surfaces do not change between the VHF and SHF regions. Finally, air damping can be ignored because the devices were measured in a vacuum for both VHF and SHF cases.

This experiment was limited to an SiO_2 layer thickness of 200 µm. The analytical solutions presented by Chandrahalim, et al.[38] provide some indications to the changes in resonator performance as the oxide layer is changed. Resonant frequency will be modified as $f_r \propto \sqrt{E_{eq}/\rho_{eq}}$, motional resistance will change as $R_m \propto E_{eq}^{1/2}\rho_{eq}^{1/2}t/Q$. The Young's modulus of SiO_2 thin films is much less than Si while their mass densities are comparable.[72] Therefore, it is expected that f_r will decrease with increasing oxide layer thickness and R_m is dependent upon both layer thickness and elasticity. These effects are demonstrated using FEA mechanical simulation and the results are presented in Figure S6 (Supporting Information). In this case, f_r and IL decrease linearly with increasing oxide layer thickness. Dielectric losses are not captured by mechanical-only FEA models. The dielectric loss tangent of AlN thin films is less than that of pure SiO_2 films.[73,74] As the thickness of the oxide layer increases, the dielectric loss due to the higher loss tangent of the oxide film will overcome the benefit of the acoustic impedance matching and reduce the device's quality factor. Future work will focus on validating this experimentally.

3. Conclusion

This paper presents a low-cost, CMOS-compatible method to enhance resonator Q factor ranging from VHF to SHF applications. Piezoelectric MEMS resonators are used in numerous engineering, aerospace, and communication systems and are used for timing, filters, sensors, and inertial navigation devices. High Q resonators are needed as higher sensitivity and resolution devices are required. Reducing the effects of system noise and interference are a key motivation of Q enhancement research.

We intentionally designed resonators to assess the Q enhancement caused by adding a silicon oxide thin film to a rectangular thin plate resonator. FEA techniques were used to evaluate resonator design operating in VHF (second CM and first WEM) and SHF (high overtone TM) vibrational modes. To validate the FEA results, an experiment was designed to demonstrate Q enhancement across a wide temperature range. The resonators were built using the PiezoMUMPs fabrication process. The S-parameters of the second CM, first WEM, and high overtone TM were measured from −200 °C to +200 °C in high vacuum conditions. Significant Q enhancement was present at VHF modes and some Q enhancement was observed in SHF modes at low operating temperatures. Q enhancement is caused by the oxide layer reducing the impedance mismatch between the dielectric and silicon layers. The Q enhancement is overcome at high frequencies and high temperatures by Akhiezer-type phonon-phonon interaction losses.

The TCF of our devices is comparable to the TCF of SiC-based resonators.[62] Furthermore, AlN is CMOS compatible and is also considered operationally stable in harsh shock, temperature, and pressure environments. This allows designers to fabricate devices on Si, which is more

© 2023 The Authors. Advanced Materials Interfaces published by Wiley-VCH GmbH

21967350, 0, Downloaded from https://onlinelibrary.wiley.com/doi/10.1002/admi.202202446 by D'Azzo Research Library, Wiley Online Library on [13/02/2023]. See the Terms and Conditions (https://onlinelibrary.wiley.com/terms-and-conditions) on Wiley Online Library for rules of use; OA articles are governed by the applicable Creative Commons License

ADVANCED MATERIALS INTERFACES
Open Access
www.advmatinterfaces.de

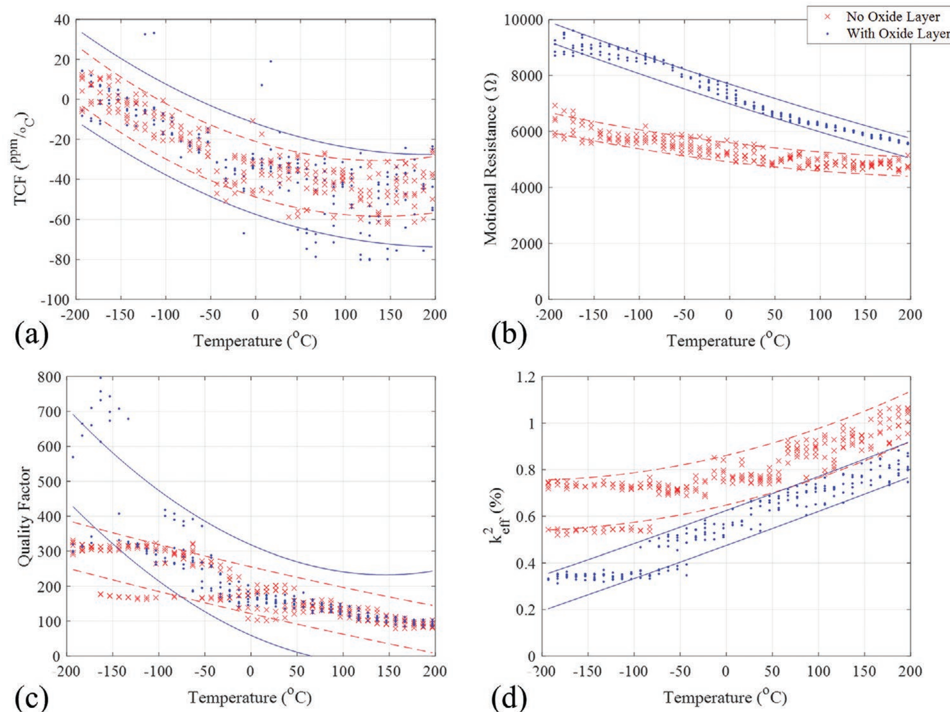

Figure 10. a) TCF, b) R_m, c) Q, and d) k_{eff}^2 of the high-overtone TM vibration at 9.65 GHz for the rectangular thin plate with the SiO_2 layer and without. Boundaries indicate the 90% confidence interval.

economical, supported by CMOS electronics, and easier to process than SiC. Thermal growth or sputtering of the SiO_2 layer can be integrated into the CMOS process. This work merits further research into other thin films that will also reduce acoustic impedance mismatch and can be incorporated into CMOS processing steps.

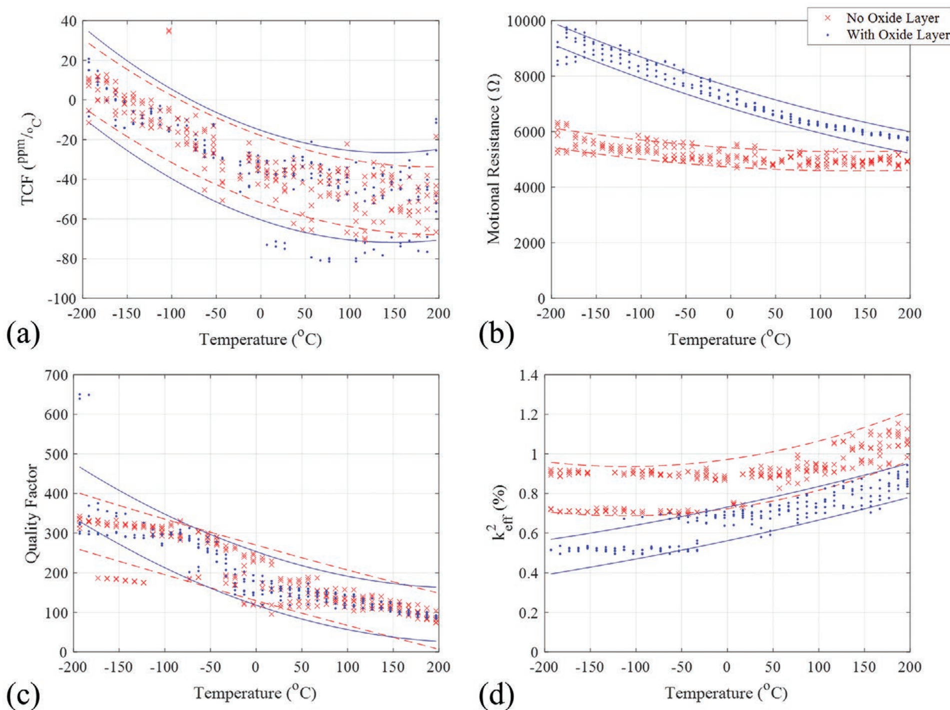

Figure 11. a) TCF, b) R_m, c) Q, and d) k_{eff}^2 of the high-overtone TM vibration at 10.0 GHz for the rectangular thin plate with the SiO_2 layer and without. Boundaries indicate the 90% confidence interval.

© 2023 The Authors. Advanced Materials Interfaces published by Wiley-VCH GmbH

21967350, 0, Downloaded from https://onlinelibrary.wiley.com/doi/10.1002/admi.202202446 by D'Azzo Research Library, Wiley Online Library on [13/02/2023]. See the Terms and Conditions (https://onlinelibrary.wiley.com/terms-and-conditions) on Wiley Online Library for rules of use; OA articles are governed by the applicable Creative Commons License

ADVANCED MATERIALS INTERFACES
Open Access
www.advmatinterfaces.de

21967350, 0, Downloaded from https://onlinelibrary.wiley.com/doi/10.1002/admi.202202446 by D'Azzo Research Library, Wiley Online Library on [13/02/2023]. See the Terms and Conditions (https://onlinelibrary.wiley.com/terms-and-conditions) on Wiley Online Library for rules of use; OA articles are governed by the applicable Creative Commons License

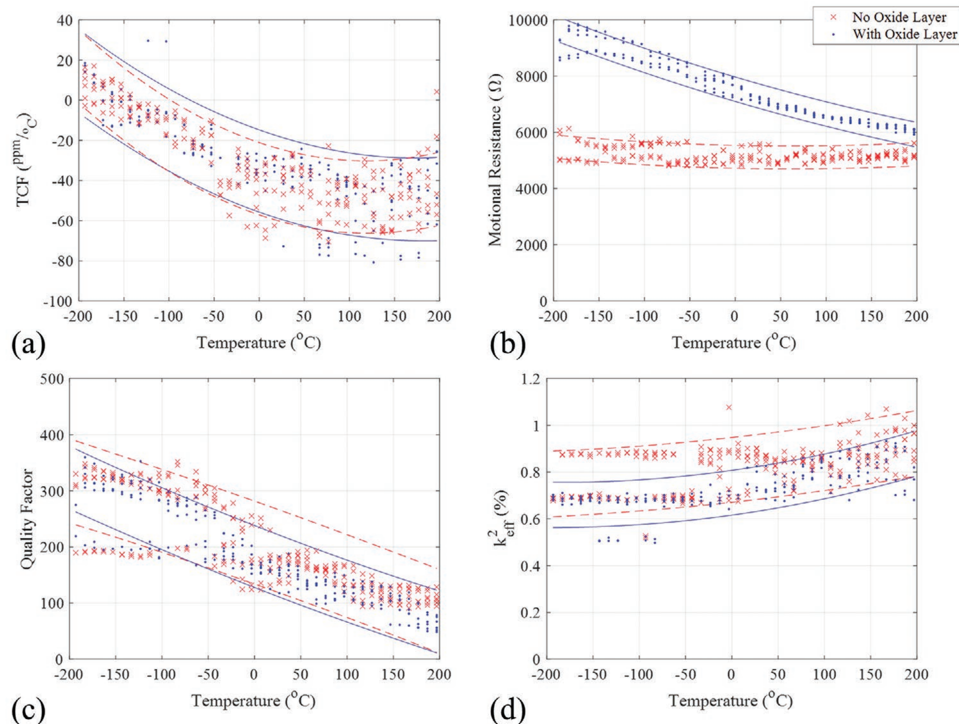

Figure 12. a) TCF, b) R_m, c) Q, and d) k_{eff}^2 of the high-overtone TM vibration at 10.35 GHz for the rectangular thin plate with the SiO_2 layer and without. Boundaries indicate the 90% confidence interval.

Table 2. Specific acoustic impedance for each layer.

Layer	Al	AlN	SiO_2	Si
Characteristic specific acoustic impedance(MPa s m^{-3})	13.6	32.5	13.1	19.7

Supporting Information

Supporting Information is available from the Wiley Online Library or from the author.

Acknowledgements

The views expressed in this paper are those of the authors and did not reflect the official policy or position of the United States Air Force, Department of Defense, or the US Government. The authors thank Mr. Adam Fritzsche and Mr. Gregory Smith for their assistance with the cryogenic probe station.

Conflict of Interest

The authors declare no conflict of interest.

Data Availability Statement

The data that support the findings of this study are available from the corresponding author upon reasonable request.

Keywords

aluminum nitride, microelectromechanical resonators, oxide interface, piezoelectric resonators, radio frequency

Received: December 7, 2022
Revised: January 25, 2023
Published online:

[1] M. Han, H. Wang, Y. Yang, C. Liang, W. Bai, Z. Yan, H. Li, Y. Xue, X. Wang, B. Akar, H. Zhao, H. Luan, J. Lim, I. Kandela, G. A. Ameer, Y. Zhang, Y. Huang, J. A. Rogers, *Nat. Electron.* **2019**, *2*, 26.
[2] G. Lee, D. Lee, J. Park, Y. Jang, M. Kim, J. Rho, *Commun. Phys.* **2022**, *5*, 94.
[3] H.-C. Song, S.-W. Kim, H. S. Kim, D.-G. Lee, C.-Y. Kang, S. Nahm, *Adv. Mater.* **2020**, *32*, 2002208.
[4] H. Chandrahalim, S. A. Bhave, R. G. Polcawich, J. Pulskamp, R. Kaul, *IEEE Electron Device Lett.* **2009**, *30*, 1296.
[5] A. Gao, K. Liu, J. Liang, T. Wu, *Microsyst. Nanoeng.* **2020**, *6*, 74.
[6] L. Hackett, M. Miller, F. Brimigion, D. Dominguez, G. Peake, A. Tauke-Pedretti, S. Arterburn, T. A. Friedmann, M. Eichenfield, *Nat. Commun.* **2021**, *12*, 2769.
[7] T. Zhang, H. Liang, Z. Wang, C. Qiu, Y. B. Peng, X. Zhu, J. Li, X. Ge, J. Xu, X. Huang, J. Tong, J. Ou-Yang, X. Yang, F. Li, B. Zhu, *Sci. Adv.* **2022**, *8*, eabk0159.
[8] D. Y. Park, D. J. Joe, D. H. Kim, H. Park, J. H. Han, C. K. Jeong, H. Park, J. G. Park, B. Joung, K. J. Lee, *Adv. Mater.* **2017**, *29*, 1702308.
[9] Z. Yi, Z. Liu, W. Li, T. Ruan, X. Chen, J. Liu, B. Yang, W. Zhang, *Adv. Mater.* **2022**, *34*, 2110291.
[10] X. Rui, Y. Li, X. Zheng, Z. Sha, Z. Zeng, *J. Phys. D: Appl. Phys.* **2019**, *52*, 355501.

© 2023 The Authors. Advanced Materials Interfaces published by Wiley-VCH GmbH

[11] F. Scinocca, A. Nabarrete, *J. Vib. Eng. Technol.* **2020**, *8*, 199.
[12] G. L. Smith, J. S. Pulskamp, L. M. Sanchez, D. M. Potrepka, R. M. Proie, T. G. Ivanov, R. Q. Rudy, W. D. Nothwang, S. S. Bedair, C. D. Meyer, R. G. Polcawich, *J. Am. Ceram. Soc.* **2012**, *95*, 1777.
[13] Q. Zhao, S. Liu, J. Chen, G. He, J. Di, L. Zhao, T. Su, M. Zhang, Z. Hou, *Rob. Auton. Syst.* **2021**, *140*, 103733.
[14] H. Kim, S. Kerrigan, M. Bourham, X. Jiang, *J. Microelectromech. Syst.* **2021**, *68*, 5346.
[15] Y. Wang, L. Qiu, Y. Luo, R. Ding, F. Jiang, *Mech. Syst. Signal Process.* **2020**, *141*, 106730.
[16] C.-C. Chu, S. Dey, T.-Y. Liu, C.-C. Chen, S.-S. Li, *J. Microelectromech. Syst.* **2017**, *27*, 59.
[17] A. Rahafrooz, S. Pourkamali, *IEEE Trans. Electron Devices* **2012**, *59*, 3587.
[18] S. Bhattacharya, S.-S. Li, *IEEE Sens. J.* **2019**, *19*, 7261.
[19] G. Pillai, S. S. Li, *IEEE Sens. J.* **2020**, *21*, 12589.
[20] T. L. Naing, T. O. Rocheleau, E. Alon, C. T. C. Nguyen, *IEEE Trans. Ultrason. Eng.* **2020**, *67*, 1377.
[21] W. T. Hsu, J. R. Clark, C. T. C. Nguyen, *IEEE Int. Conf. Micro Electro Mech. Syst.* **2001**, *00*, 349.
[22] J. R. Clark, W. Hsu, M. A. Abdelmoneum, C. T. Nguyen, *Perspective* **2005**, *14*, 1298.
[23] H. Chandrahalim, D. Weinstein, L. F. Cheow, S. A. Bhave, *Sens. Actuators, A* **2007**, *136*, 527.
[24] H. Chandrahalim, S. A. Bhave, E. Quevy, R. T. Howe, in *Aqueous transduction of poly-SiGe disk resonators* **2007**, pp. 313-316.
[25] H. Chandrahalim, S. A. Bhave, in *Proc. - IEEE Annu. Int. Conf. Micro Electro Mech. Syst.*, IEEE, New York City **2008**, 1020.
[26] F. Maita, L. Maiolo, A. Minotti, A. Pecora, D. Ricci, G. Metta, G. Scandurra, G. Giusi, C. Ciofi, G. Fortunato, *IEEE Sens. J.* **2015**, *15*, 3819.
[27] J.-H. Park, D.-G. Jang, J. W. Park, S.-K. Youm, *Sensors* **2015**, *15*, 23402.
[28] R. A. Johnson, *Mechanical Filters in Electronics*, Wiley, New York **1983**.
[29] X. Wu, L. Luo, N. Jiang, X. Wu, Q. Zheng, *Bull. Mater. Sci.* **2016**, *39*, 737.
[30] D. D. Lynes, H. Chandrahalim, J. M. Brown, K. Singh, K. T. Bodily, K. D. Leedy, *R. Soc. Open Sci.* **2022**, *9*, 211560.
[31] A. Bashir, P. H. Wöbkenberg, J. Smith, J. M. Ball, G. Adamopoulos, D. D. C. Bradley, T. Anthopoulos, *Adv. Mater.* **2009**, *21*, 2226.
[32] R. B. M. Crossa, M. M. De Souza, *Appl. Phys. Lett.* **2006**, *89*, 263513.
[33] M. Hodjat-Shamami, F. Ayazi, *Microsyst. Nanoeng.* **2020**, *6*, 108.
[34] K. Obitani, K. Araya, M. Yachi, T. Tsuchiya, *J. Microelectromech. Syst.* **2021**, *30*, 384.
[35] S. Shin, A. Daruwalla, M. Gong, H. Wen, F. Ayazi, in *2019 20th Int. Conf. Solid-State Sensors*, IEEE, New York City **2019**, pp. 503–506.
[36] H. Mansoorzare, A. Todi, S. Moradian, R. Abdolvand, *IEEE Trans. Ultrason. Eng.* **2020**, *67*, 1210.
[37] H. Chandrahalim, *Appl. Phys. Lett.* **2008**, *93*, 233504.
[38] H. Chandrahalim, S. A. Bhave, R. G. Polcawich, J. S. Pulskamp, R. Kaul, *IEEE Trans. Ultrason. Eng.* **2010**, *57*, 2035.
[39] G. Chen, M. Rinaldi, *J. Microelectromech. Syst.* **2020**, *29*, 148.
[40] R. Lu, S. Gong, *J. Micromech. Microeng.* **2021**, *31*, 114001.
[41] S. Rassay, D. Mo, C. Li, N. Choudhary, C. Forgey, R. Tabrizian, *IEEE Electron Device Lett.* **2021**, *42*, 1065.
[42] A. Ansari, M. Rais-Zadeh, *IEEE Electron Device Lett.* **2014**, *35*, 1127.
[43] G. Piazza, P. J. Stephanou, A. P. Pisano, *J. Microelectromech. Syst.* **2007**, *16*, 319.
[44] S. Das, A. Kumar, A. Kumar, J. Singh, R. Jha, M. Kumar, *IEEE Trans. Electron Devices* **2021**, *68*, 2791.
[45] X. Bian, H. Jin, X. Wang, S. Dong, G. Chen, J. K. Luo, M. J. Deen, B. Qi, *Sci. Rep.* **2015**, *5*, 1.
[46] K. Hashimoto, in *Piezoelectric MEMS Resonators* (Eds.: H. Bhugra, G. Piazza), Springer International Publishing, Cham **2017**.
[47] R. M. R. Pinto, V. Gund, R. A. Dias, K. K. Nagaraja, K. B. Vinayakumar, *J. Microelectromech. Syst.* **2022**, *31*, 500.
[48] T. Furukawa, K. Ishida, E. Fukada, *J. Appl. Phys.* **1979**, *50*, 4904.
[49] R. T. Smith, F. S. Welsh, *J. Appl. Phys.* **1971**, *42*, 2219.
[50] T. Yamada, N. Niizeki, H. Toyoda, *J. Appl. Phys.* **1967**, *6*, 151.
[51] F. Xu, S. Trolier-McKinstry, W. Ren, B. Xu, Z.-L. Xie, K. J. Hemker, *J. Appl. Phys.* **2001**, *89*, 1336.
[52] V. V. Felmetsger, P. N. Laptev, R. J. Graham, *J. Vac. Sci. Technol., A* **2011**, *29*, 021014.
[53] S. Shahraini, H. Mansoorzare, A. Mahigir, R. Abdolvand, *J. Microelectromech. Syst.* **2020**, *29*, 296.
[54] J. Wang, M. Park, S. Mertin, T. Pensala, F. Ayazi, *J. Microelectromech. Syst.* **2020**, *29*, 741.
[55] C. Fei, X. Liu, B. Zhu, D. Li, X. Yang, Y. Yang, Q. Zhou, *Nano Energy* **2018**, *51*, 146.
[56] G. Piazza, V. Felmetsger, P. Muralt, R. H. I. Olsson, R. Ruby, *MRS Bull.* **2012**, *37*, 1051.
[57] S. Dey, S. Jejurikar, S. K. Bhattacharya, A. Banerji, K. P. Adhi, C. V. Dharmadhikari, *J. Appl. Phys.* **2010**, *108*, 094510.
[58] J. F. Clawson, G. T. Tsuyuki, B. J. Anderson, C. G. Justus, W. Batts, D. Ferguson, D. G. Gilmore, in *Spacecraft Thermal Control Handbook*, 2nd ed. (Eds: D. G. Gilmore), The Aerospace Press, El Segundo, CA **2002**, Ch. 2.
[59] H. R. Shea, in *Proc. Reliability, Packaging, Testing, and Characterization of MEMS/MOEMS and Nanodevices X* (Eds.: S. Garcia-Blanco, R. Ramesham) SPIE, Bellingham, Washington, USA **2011**.
[60] N. D. Patel, P. S. Nicholson, *NDT Int.* **1990**, *23*, 262.
[61] Y. Seo, D. Kim, N. A. Hall, *J. Microelectromech. Syst.* **2019**, *28*, 271.
[62] W. Sui, H. Wang, J. Lee, A. Qamar, M. Rais-Zadeh, P. X.-L. Feng, *Adv. Funct. Mater.* **2022**, *32*, 2202204.
[63] G. Piazza, P. J. Stephanou, A. P. Pisano, *J. Microelectromech. Syst.* **2006**, *15*, 1406.
[64] A. D. Matyushov, B. Spetzler, M. Zaeimbashi, J. Zhou, Z. Qian, E. V. Golubeva, C. Tu, Y. Guo, B. F. Chen, D. Wang, A. Will-Cole, H. Chen, M. Rinaldi, J. McCord, F. Faupel, N. X. Sun, *Adv. Mater. Technol.* **2021**, *6*, 2100294.
[65] O. Brand, I. Dufour, S. M. Heinrich, F. Josse, *Resonant MEMS: Fundamentals, Implementation, and Application* **2015**.
[66] A. Cowen, G. Hames, K. Glukh, B. Hardy, *MEMSCAP Inc* **2014**.
[67] J. Rodriguez, S. A. Chandorkar, C. A. Watson, G. M. Glaze, C. H. Ahn, E. J. Ng, Y. Yang, T. W. Kenny, *Sci. Rep.* **2019**, *9*, 2244.
[68] K. Y. Yasumura, T. D. Stowe, E. M. Chow, T. Pfafman, T. W. Kenny, B. C. Stipe, D. Rugar, *J. Microelectromech. Syst.* **2000**, *9*, 117.
[69] L. E. Kinsler, A. R. Frey, A. B. Coppens, J. V. Sanders, *Fundamentals of Acoustics*, 4th ed., Wiley, New York **2000**.
[70] R. Tabrizian, M. Rais-Zadeh, F. Ayazi, in *Int. Conf. Solid-State Sensors, Actuators Microsystems*, IEEE, New York City **2009**, pp. 2131–2134.
[71] A. Akhiezer, *J. Phys.* **1939**, *1*, 277.
[72] M. T. Kim, *Thin Solid Films* **1996**, *283*, 12.
[73] J. S. Thorp, D. Evans, M. Al-Naief, M. Akhtaruzzaman, *J. Mater. Sci.* **1990**, *25*, 4956.
[74] D. Li, J. Gao, J. E. Austermann, J. A. Beall, D. Becker, H. M. Cho, A. E. Fox, N. Halverson, J. Henning, G. C. Hilton, J. Hubmayr, K. D. Irwin, J. Van Lanen, J. Nibarger, M. Niemack, *IEEE Trans. Appl. Supercond.* **2013**, *23*, 23.

© 2023 The Authors. Advanced Materials Interfaces published by Wiley-VCH GmbH

21967350, 0, Downloaded from https://onlinelibrary.wiley.com/doi/10.1002/admi.202202446 by D'Azzo Research Library, Wiley Online Library on [13/02/2023]. See the Terms and Conditions (https://onlinelibrary.wiley.com/terms-and-conditions) on Wiley Online Library for rules of use; OA articles are governed by the applicable Creative Commons License

ADVANCED MATERIALS INTERFACES

Supporting Information

for *Adv. Mater. Interfaces,* DOI: 10.1002/admi.202202446

Influence of a Tailored Oxide Interface on the Quality Factor of Microelectromechanical Resonators

David D. Lynes and Hengky Chandrahalim**

Supporting Information

Influence of a tailored oxide interface on the quality factor of microelectromechanical resonators

David D. Lynes and Hengky Chandrahalim

Department of Electrical and Computer Engineering

Air Force Institute of Technology,

Wright-Patterson Air Force Base, OH 45433, USA

S.1 FEA Simulations

Table S1. Layer bulk properties.

Layer	Density (kg m^{-3})	Young's modulus (GPa)	Acoustic Velocity (m s^{-1})
Al	2700	69	5055
AlN	3260	325	9984
SiO_2	2465	70	5325
Si	2330	166	8440

FEA simulations are accomplished with Ansys Mechanical using the material parameters listed in Table S1. To predict the behavior of the 2nd CM and 1st WEM vibrations, three-dimensional models are used. The three-dimensional models are bisected along the longitudinal line of symmetry for computing efficiency. Frictionless boundary conditions are assigned at the bisection and fixed boundary conditions are assigned to the ends of the anchors. Illustrations of the three-dimensional FEA models are presented in Figure S1. A two-dimensional FEA model is used to predict the behavior of high overtone TM vibrations. In this case, the model represents a cross sectional cut of the rectangular thin plate and both ends are constrained by frictionless boundary conditions. Illustrations of the two-dimensional FEA models are presented in Figure S2. Harmonic analysis is performed and S-parameters are extracted from the calculated stress on the AlN geometry. S21 obtained from FEA results for the 2nd CM and 1st WEM are reported in Figure S3 (a) and three high overtone TM vibrations operating in the SHF spectrum are reported in Figure S3 (b). Resonant frequency (f_r) values as predicted by FEA are presented in Table S2.

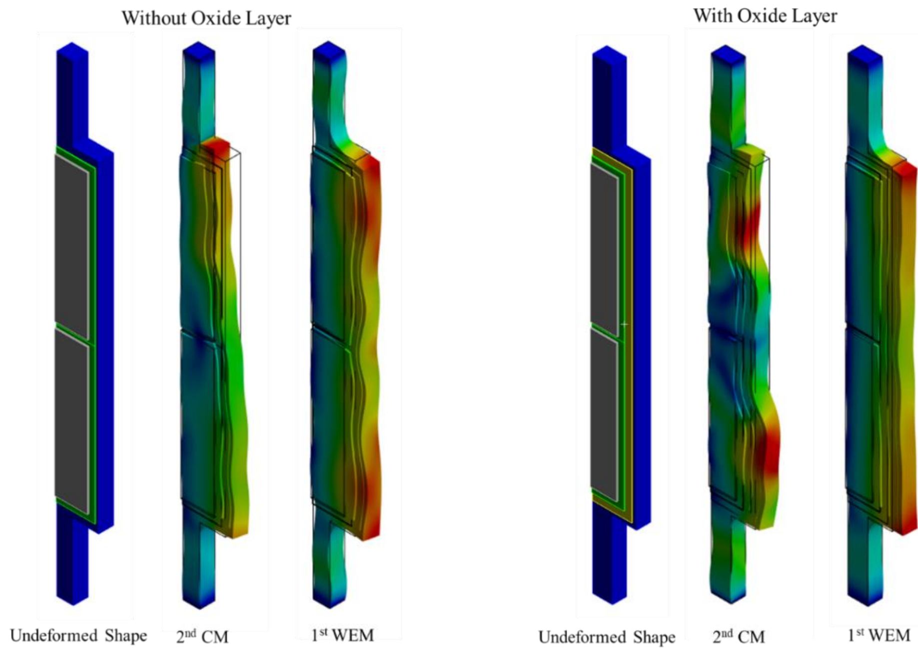

Figure S1. Three dimensional FEA models for rectangular thin plate resonators with and without an oxide layer. Deformed shapes are presented for 2nd CM and 1st WEM. Deformations are not to scale.

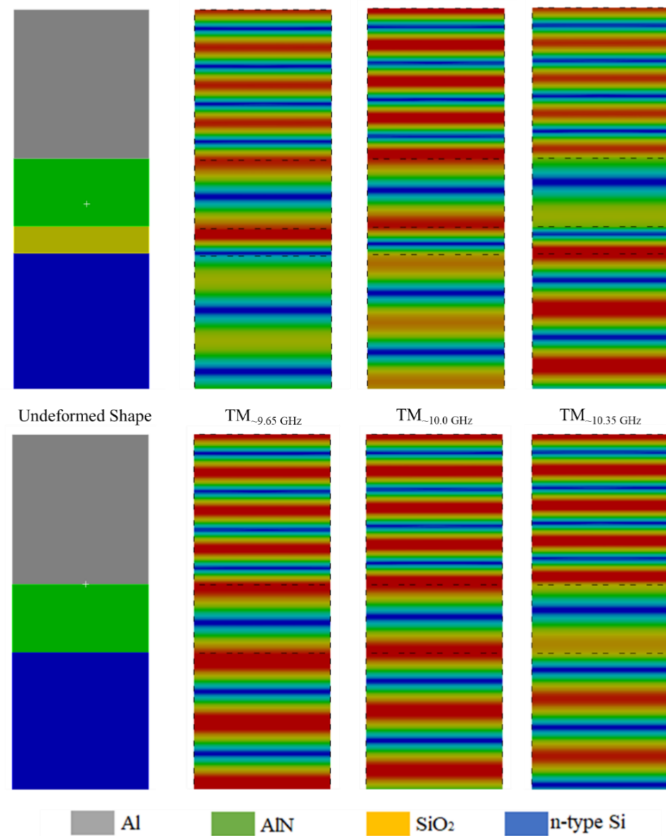

Figure S2. Two dimensional FEA models and deformed shapes for high overtone TM vibrations operating in the SHF spectrum.

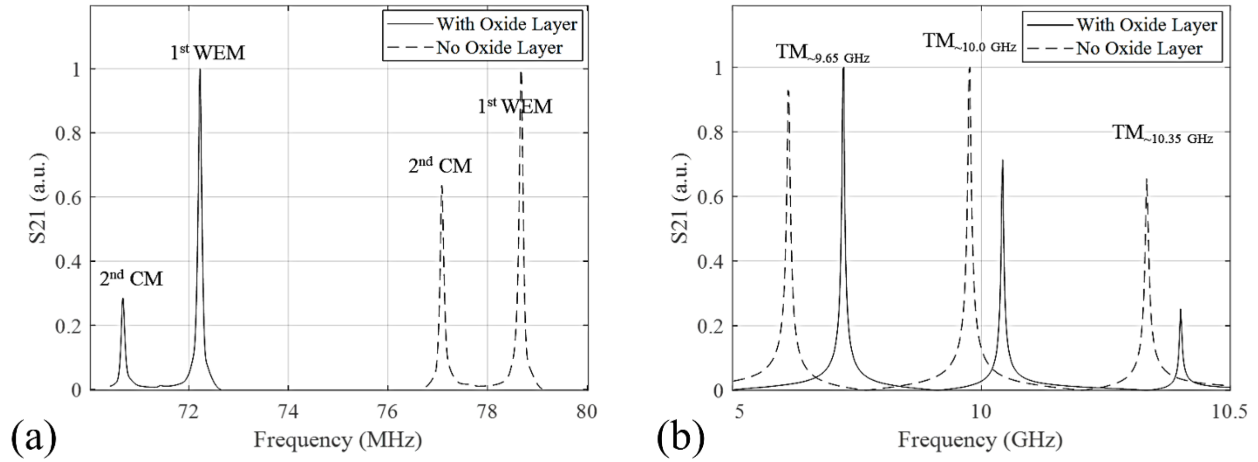

Figure S3. Harmonic response results obtained from Ansys Mechanical. (a) Results for 2nd CM and 1st WEM vibrations. (b) Results for high overtone TM vibrations.

Table S2. Vibrational modes and corresponding resonant frequencies obtained from FEA simulations.

Mode	f_r No Oxide Layer	f_r With Oxide Layer
2nd CM	77.08 MHz	70.68 MHz
1st WEM	78.68 MHz	72.23 MHz
$TM_{\sim 9.65\ GHz}$	9.61 GHz	9.72 GHz
$TM_{\sim 10.0\ GHz}$	9.98 GHz	10.04 GHz
$TM_{\sim 10.35\ GHz}$	10.33 GHz	10.40 GHz

S.2 Fabrication

The resonator designs were fabricated using MEMSCap's process in accordance with the PiezoMUMPs design rules.[1] The PiezoMUMPs design flow is summarized in Figure S4. The substrate is a 150 mm (100) oriented silicon-on-insulator (SOI) wafer. The silicon layer is n-doped with phosphorous to increase conductivity. A thermal oxide layer is grown and wet etched. Then, the AlN thin film is deposited by reactive sputtering and wet-etched. Next, 20 nm chrome and 1000 nm Al are deposited and patterned by a lift-off process. The n-doped Si and thermal oxide

layers are lithographically patterned and etched by reactive ion etching (RIE). Finally, the devices are released by back-etching the handle wafer by a combination of RIE and wet oxide etch.[1] Scanning electron microscope cross-sectional images of the completed stack are shown in Figure S5. The imagery indicates the layers are uniform and well defined.

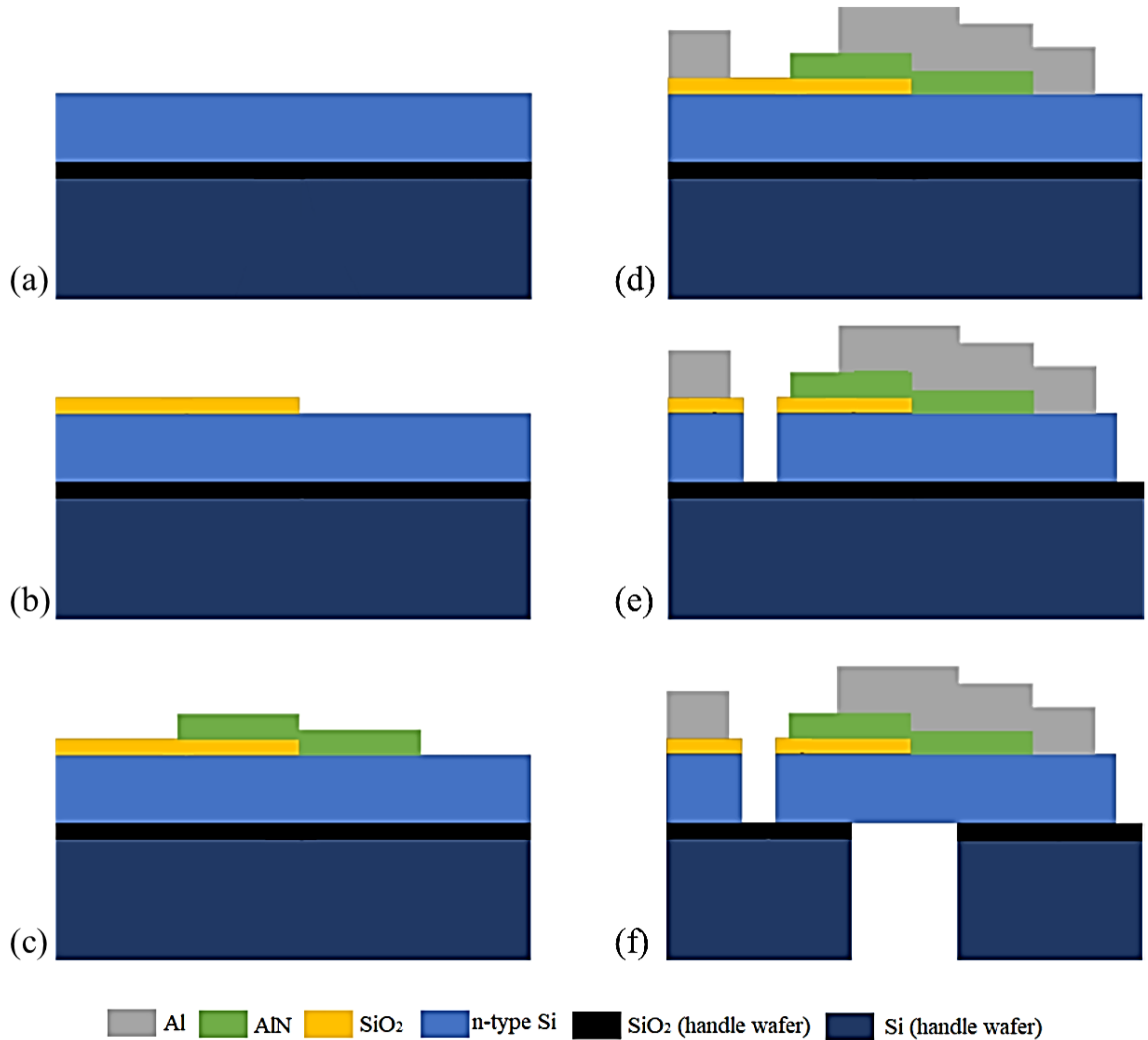

Figure S4. Summary of PiezoMUMPs fabrication process flow. (a) Top Si layer of SOI wafer is n-doped with phosphorous. (b) Growth and patterning of thermal oxide layer. (c) Deposition and patterning of piezoelectric AlN layer. (d) Deposition and patterning of conducting Al layer. (e) RIE of thermal oxide and n-type Si. (f) Backside RIE of substrate Si and oxide layers.

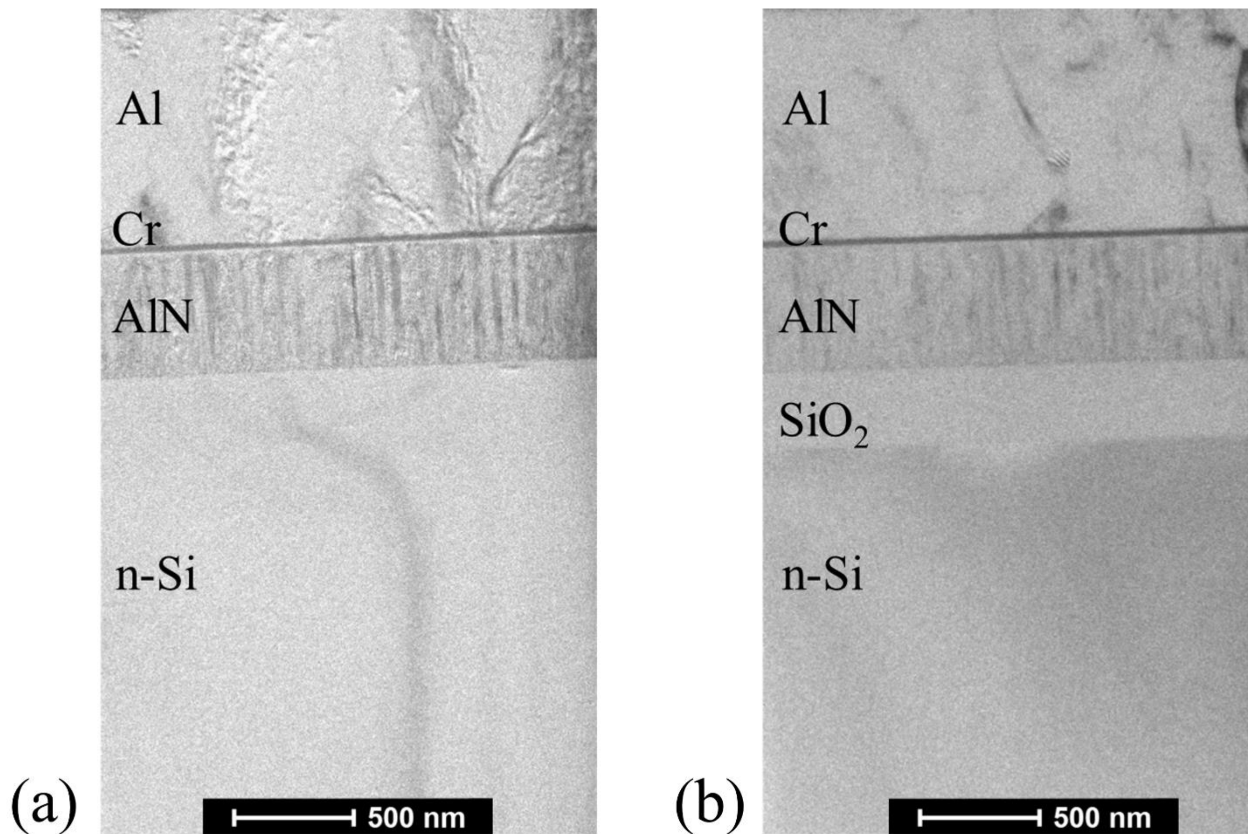

Figure S5. SEM cross-sectional images of (a) the AlN-on-Si and (b) AlN-on-SiO_2 designs.

S.3 Effects of Oxide Layer Thickness

The thickness of the SiO_2 layer can be controlled during fabrication. The effects of altering the thickness of the oxide layer are studied using FEA mechanical simulation. The results are presented in Figure S6. In the case of the AlN-on-SiO_2 BAW resonator operating in the width extensional mode, f_r and IL decrease linearly with increasing oxide layer thickness. The parametric study was performed using ANSYS Mechanical, which does not include dielectric or piezoelectric loss effects.

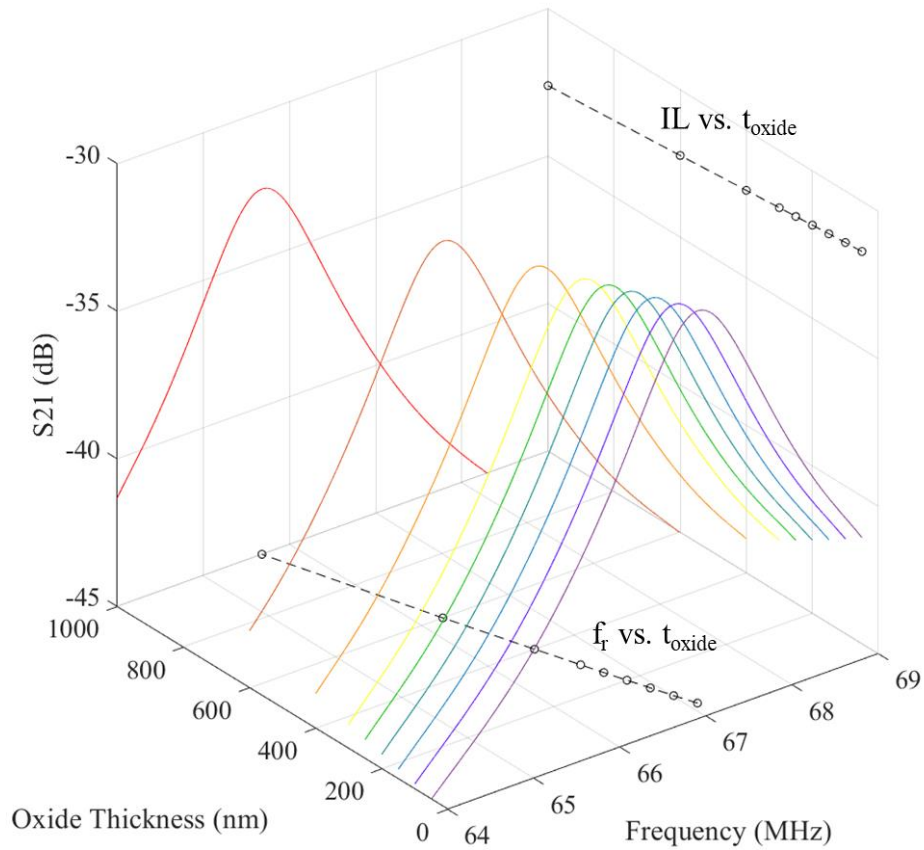

Figure S6. Results of FEA parametric study of the harmonic response as a function of oxide layer thickness. Simulation results show f_r and IL decrease linearly with increasing oxide layer thickness.

References

[1] A. Cowen, G. Hames, K. Glukh, B. Hardy, *MEMSCAP Inc* **2014**, *1*.